Turkish Journal of Physics

http://journals.tubitak.gov.tr/physics/

Research Article

Turk J Phys
(2018) 42: 573 – 586
© TÜBİTAK
doi:10.3906/fiz-1802-19

# The effects of X-ray background on the X-ray emission from the Galactic supernova remnants

**Nergis CESUR**[1,2*], **Aytap SEZER**[3], **Murat HÜDAVERDİ**[2]

[1]Graduate School of Natural and Applied Sciences, Yıldız Technical University, İstanbul, Turkey
[2]Department of Physics, Yıldız Technical University, İstanbul, Turkey
[3]Department of Electrical and Electronics Engineering, Faculty of Engineering and Architecture, Avrasya University, Trabzon, Turkey

**Received:** 11.02.2018 • **Accepted/Published Online:** 19.07.2018 • **Final Version:** 12.10.2018

**Abstract:** We present the results of an X-ray background emission study of the well-known Galactic supernova remnants (SNRs) Cas A, RCW 86, RX J1713.7−3946, and SN 1006 by using the archival Chandra and XMM-Newton X-ray Observatories data. With the advent of detector technologies and increased capability of the spectral resolutions, accurate background modelling for the extended sources, such as SNRs, is getting crucial at the modelling step since it might be effective on estimating the physical parameters of the plasma. For this purpose, we concentrate on the background emission spectral modelling by investigating its spectral parameters and components. Hence, the results of the modelled background spectra of these four SNRs are presented by using the combination of thermal and nonthermal emission models properly to the background components.

**Key words:** X-rays, interstellar medium, supernova remnants, X-ray background

## 1. Introduction

Analysing the extended and faint sources, such as the Galactic supernova remnants (SNRs), with accurately modelled background emission is important since it might affect the spectral results (e.g., [1,2,3]). The location of an SNR in the sky (e.g., Galactic latitude) is critical for the background estimation, which will define the model fraction of the cosmic X-ray background (CXB), the Galactic ridge X-ray emission (GRXE), or the foreground emission (FE) (see Figure 1 for a simulated projection[1]). Moreover, in recent years, the importance of background modelling before performing detailed spectral analysis has been emphasised in plenty of studies (e.g., [3,4,5,6]). Under these circumstances, all spectral parameters can be examined reliably with the background modelling method, which is suitable for determining the thermal or nonthermal characteristics of SNRs. In this paper, we aimed to investigate the X-ray background emission of the well-known Galactic SNRs Cas A, RCW 86, RX J1713.7−3946, and SN 1006 with various approaches according to their X-ray background conditions. For this purpose, we used archival Chandra and XMM-Newton data.

The background components are described briefly in Section 2. The observations and data reduction steps are described in Section 3. In Section 4, the analysis results are reported in detail, and we discuss the effect of the background components for each SNR. We summarise our main conclusions in Section 5.

*Correspondence: nergis.cesur.507@std.yildiz.edu.tr

[1]https://www.mrao.cam.ac.uk/surveys/snrs/snrs.frame.html

This work is licensed under a Creative Commons Attribution 4.0 International License.

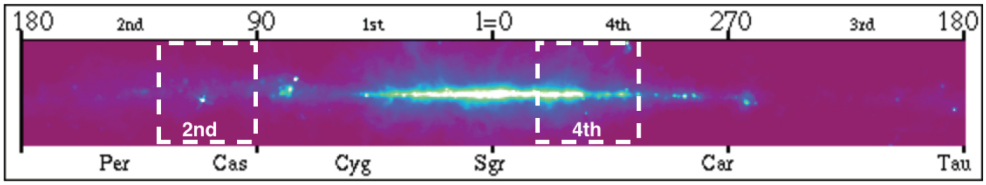



**Figure 1**. Roughly estimated positions of the SNRs on the Galactic plane at 408 MHz. Cas A is in the $2^{nd}$ quadrant; RCW 86, SN 1006, and RX J1713.7−3946 are in the $4^{th}$ quadrant [7].

**Table 1**. The background component information for each SNR studied.

| SNR | Galactic Coord. | Observatory | Obs. Id. | Exposure | Background |
|---|---|---|---|---|---|
| | *(l,b)* | | | (ks) | Components |
| Cas A | 111°.7347, – 02°.1296 | Chandra | 4639 | 80 | CXB + GH + FE |
| RCW 86 | 315°.0927, – 02°.3765 | XMM-Newton | 0504810401 | 73 | CXB + FE |
| RX J1713.7−3946 | 347°.2695, – 00°.2569 | Chandra | 5561, 12671 | 29, 91 | CXB + GRXE + FE |
| SN 1006 | 327°.4109, + 14°.4674 | Chandra | 13737, 13742 | 74, 80 | CXB + LHB |
| | | | 13741, 13739 | 88, 99 | |
| | | | 13738 | 101 | |

## 2. A brief introduction to background components

### 2.1. Galactic ridge X-ray emission

Most of the GRXE has a diffuse origin [8,9]. Its spectrum is hard and contains many emission lines of the most abundant elements [10]. If an SNR is located near the Galactic disc, the background is dominated by the GRXE; thus, the emission lines of elements such as Mg, Si, S, and Fe will be expected from the background spectra as well as a hard continuum [5,11,12]. Generally, the GRXE spectrum is represented by the sum of the high- and low-temperature plasma of the collisional ionisation equilibrium (CIE) model (APEC in Xspec) [11] with a free absorption parameter, plus a nonthermal X-ray emission with a photon index of approximately 2 with neutral Fe lines at 6.4 keV of equivalent width 0.46 keV and at 7.06 keV [5]. Ebisawa et al. [10] discovered the K$\alpha$ line of neutral Fe in the spectrum of the GRXE. The flux of the GRXE depends on the Galactic latitude [5,11], and it extends over several tens of degrees along the Galactic plane, where it becomes brighter through the Galactic centre with a total luminosity of approximately $10^{38}$ erg s$^{-1}$ [13]. According to a previous study [5], the GRXE spectrum requires the following components: the high-temperature plasma (HP; responsible for the 6.7 keV line), which probably originates from cataclysmic variables; the low-temperature plasma (LP; responsible for the 2.45 keV line), which may originate from multiple supernovae (SNe) within the past $10^5$ yr or point sources like dM stars; the cold matter (CM; might be responsible for the 6.4 keV line), which possibly originates from the bombardment of X-rays or particles in cold interstellar gas; plus, the FE (dominates below 2 keV band). Moreover, the study [5] suggests that neutral Fe K$\alpha$ line is caused by the absorption parameter, which is the intra-cloud absorption. However, the origin of this line is not clear yet. On the other hand, while estimating the GRXE background, in some cases, the separating to the component method is not always adhered to according to some sources (e.g., [6,14,15]).

### 2.2. Cosmic X-ray background

The CXB can be defined as the integrated emission of all the extragalactic sources and it dominates the hard X-ray surface brightness. Moreover, it has been resolved into several sources [16,17]. It depends very little on

the Galactic coordinates. The varied measurements of the CXB in $0.3-10$ keV band of various high resolution X-ray telescopes showed that the primary contributor to the extra-galactic CXB is the integrated emission of the Active Galactic Nuclei (AGN) background. In a very recent study [18], Cappelluti et al. found that 10% of the CXB is produced by accretion onto early black holes. In the same study, they found a thermal contribution below 1 keV, which originates $0.5-2$ keV flux, but approximately $8-11$% of this fragment cannot be explained by either resolved or unresolved X-ray sources, and the spectrum has a photon index value of approximately 2.1 [17,18]. The CXB emission consists of approximately two components, and this thermal contribution is the first one and it was found that its origin is totally Galactic [17]. The other one is the hard-band emission ($\sim 2-10$ keV) and the spectrum of this emission is characterised by a power-law (PL) spectrum, which has a photon index value of approximately 1.41 and its contribution to the Galaxy is $3-7$% [17]. Similarly, the method of Kushino et al. [17] is the most commonly used one for modelling the CXB spectrum of the Galactic SNRs, which dominates the hard X-ray surface brightness. In their study [17], Kushino et al. obtained a photon index of approximately 1.41, and the surface brightness value of approximately $5.41 \times 10^{-15}$ erg s$^{-1}$ cm$^{-2}$ arcmin$^{-2}$ for $2-10$ keV hard-band emission power-law component. While calculating the flux of the nonthermal CXB component with the surface brightness value mentioned, effective area ratios between the source and the background regions for each energy bin should be multiplied to correct the vignetting effect of the background spectrum.

### 2.3. Foreground emission

A low energy emission ($\leq 2$ keV) indicates a very weak or no absorption at all, unrelated to Galactic Center region. Its origin is unknown but reported to be a local Galactic plasma or unresolved dM stars [19]. In a previous study [19], it was shown that the FE dominates below the 2 keV energy, especially in the Galactic centre region. FE is generally represented by the CIE model (APEC) whether with negligible absorption parameter (e.g., [20,21]) or with absorbed two thin plasma temperature CIE model in the GRXE component (e.g., [2,5]), where its emission is a few percent of that GRXE [13]. As we follow the local hot bubble map in [22] and take into account the Galactic locations of the SNRs, the relative contributions or domination of the local hot bubble to the FE is arbitrary for our selected SNRs except SN 1006. However, as in [21], in order to model the FE spectra, the local hot bubble type spectral model was used. Note that the true origin of FE is not known accurately; thus, in our analysis, we applied the model which gives a reasonable fit to the data as in [23]. For this reason, some apparent properties of its contributors should not be taken seriously.

### 2.4. Local hot bubble

The local hot bubble (LHB) is an irregular local cavity filled with X-ray emitting hot gas ($10^6$ K) of approximately 100 pc at a reasonable pressure that could produce observed local X-rays, which is in the foreground, and displaces the cool gas. Moreover, it shows no absorption by cool interstellar gas, and it is in CIE and thus can be modelled by an unabsorbed thermal component (APEC) [22,24]. The lower absorption of the LHB is attributed to higher X-ray emitting directions, where it might be greater in extent, and hence there is less cool gas in these locations [24]. In a previous study [1], unabsorbed contribution of the LHB was fitted with a $kT_e$ value of 0.7 keV. On the other hand, in another study [25], the LHB was fitted with a $kT_e$ value of about 0.105 keV. Note that the Galactic location of the SNR might be the determinant of this variation [22].

### 2.5. Galactic halo

The Galactic halo (GH) plasma is assumed to be in CIE, so the APEC model is used [20]. According to the $0.1-1.0$ keV diffuse soft X-ray background observations, it is a $(1-3) \times 10^6$ K plasma in the halo of the Galaxy beyond the main Galactic disc [20,26] and tends to increase from the outer to the inner Galaxy [20]. Furthermore, in their study [20], Henley and Shelton reported that the emission of the halo increases weakly with the latitude in the north and is not correlated with the latitude in the south. Yoshino et al. [26] found in their study that the halo emission decreases with increasing latitude, and this result is contrary to that reported in [20]. Although the origin of this hot halo gas is uncertain, there are two assumptions of the main process: SN-driven outflows from the Galactic disc and the accretion of the material from the intergalactic medium (see the references [20]). In a previous study [27], it was estimated as a hard component with an absorbed nonequilibrium ionisation (NEI) model with a temperature of 0.3 keV.

## 3. Analysis

### 3.1. X-ray observations and data reduction

In each analysis, Heasoft 6.20[2], CALDB 4.7.2[3], CIAO 4.9[4], XMM-SAS 16.0.0[5], Xspec 12.9.1[6], SAOImage DS9 7.5[7], AtomDB 3.0.9[8], and the up-to-date versions of the current calibration files (CCFs)[9] were used.

As in the standard procedure by Chandra X-ray Center[10], the event list Chandra files are gathered by ACIS-S and ACIS-I, reprocessed by using the script CHANDRA_REPRO, and for restricting the energy ranges and creating the images, DMCOPY script is used on the event files, respectively. Ancillary Response Files (ARFs) and Response Matrix Files (RMFs) are generated with SPECEXTRACT script in CIAO. In this paper, only the XMM-Newton data for RCW 86 were analysed, which cover the SNR shell region and provide an opportunity to select a larger emission free area in same field of view (FoV) in comparison with the Chandra data. Since we focused on the emphasis of the background estimation, selecting a larger background region is a preferable way for a general approach to get a statistically acceptable fit with sufficient counts. For the spectral analysis of XMM-Newton observation, EPIC-MOS data were used. X-ray events corresponding to patterns $0-12$ and flag $= 0$ for MOS1/2 were selected. The metatask EMCHAIN included in ESAS package integrated into SAS, were used to identify good time intervals, filter, and create new clean event files. After this process, SAS task EVIGWEIGHT was used for vignetting-weighted event lists for each EPIC instrument to correct for the effective area variation across the SNR [28]. Spectral files were created with EVSELECT task, ARFs were created with ARFGEN task, and RMFs were created with RMFGEN task in SAS. The MOS1 CCD6 was damaged by micrometeorite events; thus, it was no longer recording observations, this is where some of the SNR area falls on that CCD[11]. Hence, the data of that EPIC instrument were not used.

In the spectral analysis with Xspec, the solar abundance table in [29] was adopted. Unless otherwise specified, all errors represent 90% confidence level. Note that the abbreviations N, S, NW, SE, SW, and

[2] https://heasarc.nasa.gov/lheasoft/
[3] http://cxc.harvard.edu/caldb/
[4] http://cxc.harvard.edu/ciao/index.html
[5] https://www.cosmos.esa.int/web/XMM-Newton/sas
[6] https://heasarc.gsfc.nasa.gov/xanadu/xspec/
[7] http://ds9.si.edu/site/Home.html
[8] http://www.atomdb.org
[9] https://www.cosmos.esa.int/web/XMM-Newton/current-calibration-files
[10] http://cxc.harvard.edu
[11] https://www.cosmos.esa.int/web/XMM-Newton/mos1-ccd6

W represent North, South, Northwest, Southeast, Southwest, and West that are used for naming the rims, respectively. The background components and observational information for each SNR can be seen in Table 1.

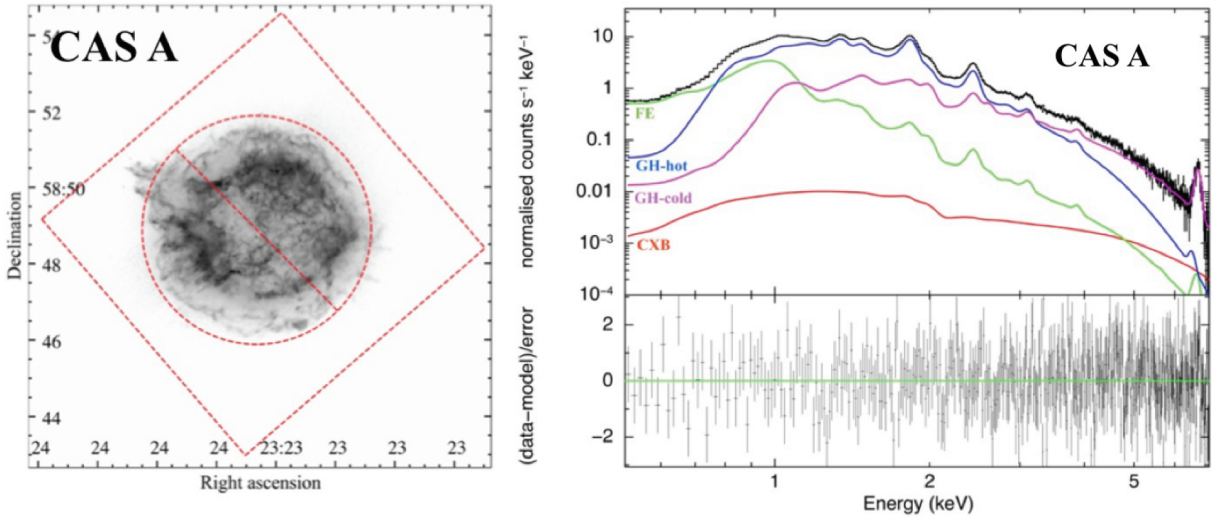



**Figure 2**. *Left*: The selected background region for Cas A. *Right*: The background spectrum of Cas A. The coloured lines indicate the contribution of the various components to the spectrum.

**Table 2**. Best-fit parameters for the background spectrum of Cas A.

| Components | Parameters | Values |
|---|---|---|
| CXB | | |
| | $N_H$ ($10^{22}$ cm$^{-2}$) ‡ | 0.394 *(fixed)* |
| | Photon index † | 1.412 *(fixed)* |
| | S. B. † (erg s$^{-1}$ cm$^{-2}$ arcmin$^{-2}$) | $5.410 \times 10^{-15}$ *(fixed)* |
| *FE* | | |
| | kT$_e$ (keV) | $1.074 \pm 0.004$ |
| | Norm ($10^{-2}$ cm$^{-5}$) | $0.325 \pm 0.006$ |
| *GH-hot & GH-cold* | | |
| | $N_H$ ($10^{22}$ cm$^{-2}$) | $2.115 \pm 0.007$ |
| | kT$_e$ (keV) ‖ | 0.658 *(fixed)* |
| | Norm (cm$^{-5}$) | $0.373 \pm 0.003$ |
| | kT$_e$ (keV) ‖ | 1.500 *(fixed)* |
| | Norm ($10^{-2}$ cm$^{-5}$) | $4.964 \pm 0.007$ |
| | $\chi^2$ / d.o.f | 434.23 / 439 |

*S. B.: Surface Brightness in the 2 − 10 keV band, †: [17].*
*‡:[30].*
*‖:[31].*
*The normalisation of the* APEC, *norm* $= 10^{-14} \int n_e n_H dV / (4\pi d^2)$, *where* $n_e$, $n_H$, $V$, *and* $d$ *are the electron and hydrogen densities* (cm$^{-3}$), *emitting volume* (cm$^3$), *and distance to the source* (cm), *respectively.*

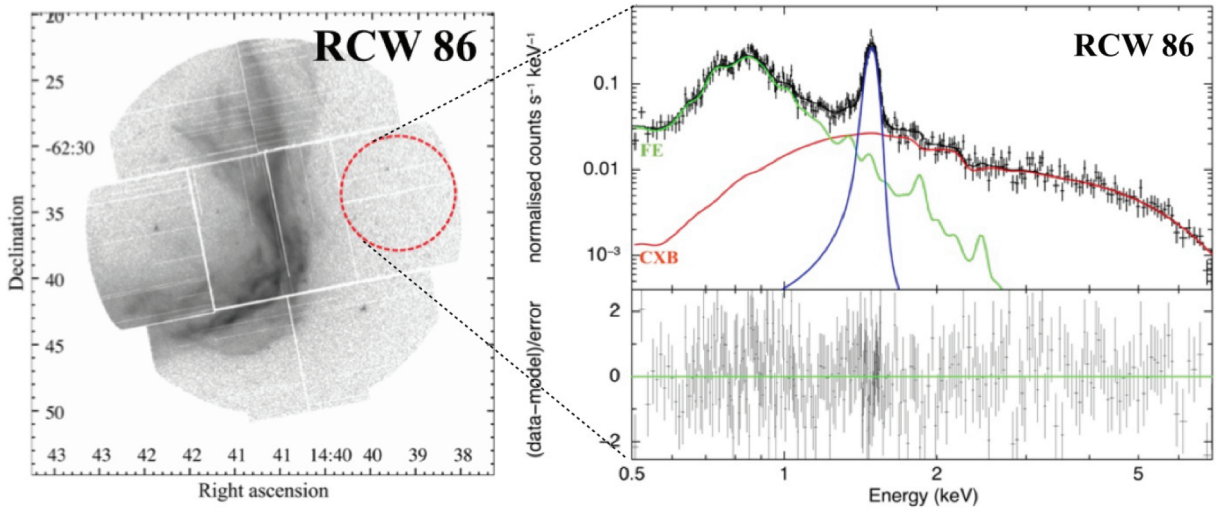



**Figure 3**. *Left*: The selected background region for RCW 86. *Right*: The background spectrum of RCW 86. The blue line indicates the contribution of the instrumental self-fluorescence line of aluminium (1.49 keV).

### 3.2. X-ray spectral analysis of the selected background regions of the SNRs

The CXB component parameters of all the background regions were fixed with a power-law shape at a photon index of 1.41 and a surface brightness of 5.41 $\times$ $10^{-15}$ erg $s^{-1}$ $cm^{-2}$ $arcmin^{-2}$ as those in [17]. All of the thermal background contribution of each component was fitted with the APEC. In order to calculate the absorption parameter, TBABS model was used [29], and the hydrogen column density parameter of the CXB component was fixed at a significant value as in [15]. These values are indicated in the relevant tables. The background spectra were simulated by using the FAKEIT command in Xspec, and then they were ready to be subtracted from the source spectra. For multiple rims, we used one of them as sample to give an example for the spectral characteristic.

**Table 3**. Best-fit parameters for the background spectrum of RCW 86.

| Components | Parameters | Values |
|---|---|---|
| *CXB* | | |
| | $N_H$ ($10^{22}$ $cm^{-2}$) ‡ | 0.723 *(fixed)* |
| | Photon index | 1.412 *(fixed)* |
| | S. B. † (erg $s^{-1}$ $cm^{-2}$ $arcmin^{-2}$) | 5.410 $\times$ $10^{-15}$ *(fixed)* |
| *FE* | | |
| | $kT_e$ (keV) | 0.703 $\pm$ 0.014 |
| | Norm ($10^{-2}$ $cm^{-5}$) | 0.037 $\pm$ 0.010 |
| | $\chi^2$ / d.o.f | 256.89 / 258 |

†: *[17]*. ‡:*[30]*.

The background region for Cas A, was extracted from a rectangular area of 39.53 $arcmin^2$ in the same FoV, where the whole SNR region data with a circular area of 28.27 $arcmin^2$ is excluded (as seen in Figure 2). The

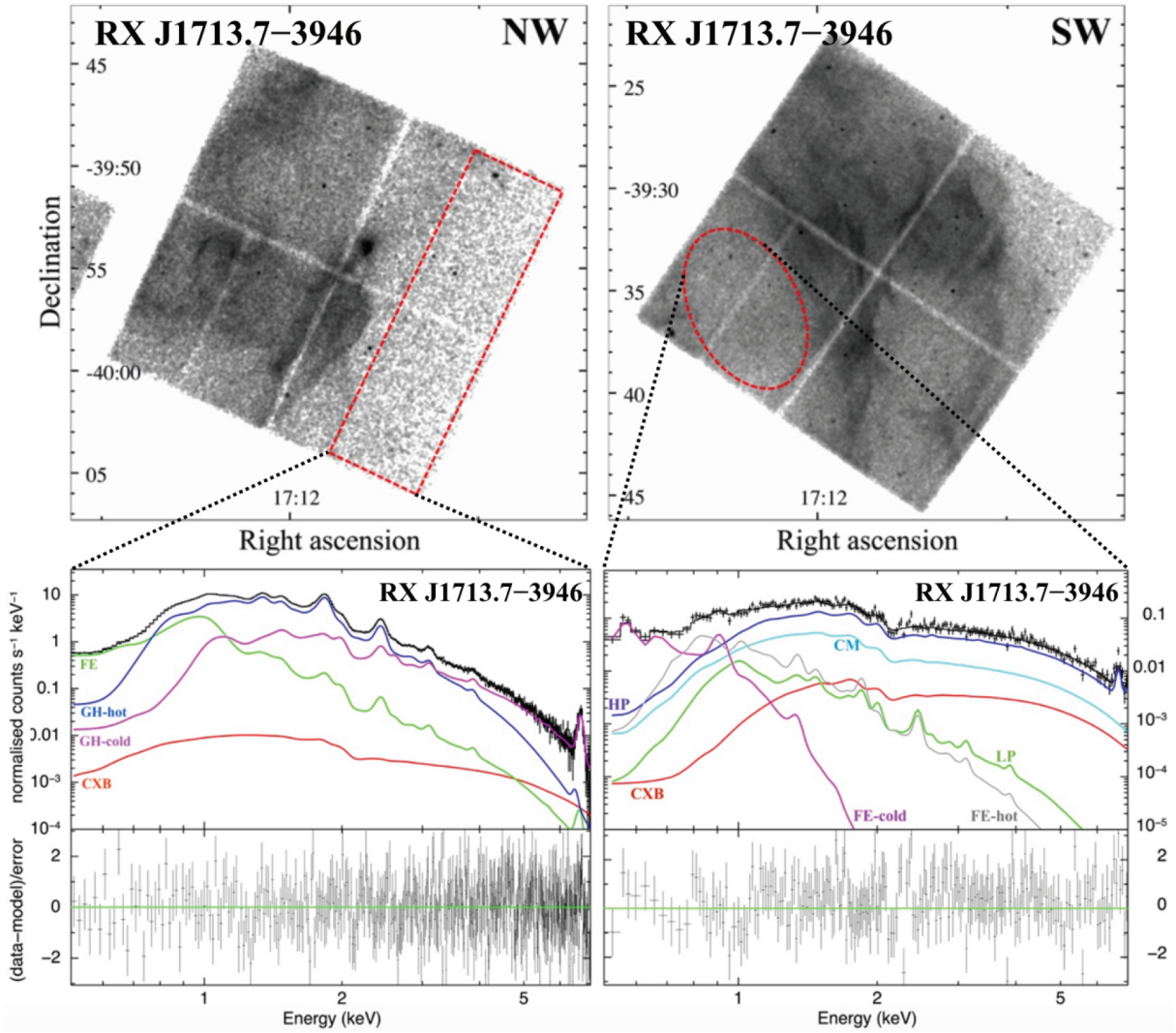



**Figure 4**. *Top*: The selected background regions for RX J1713.7 − 3946. *Bottom*: The background spectra of the SW and the NW rims of RX J1713.7 − 3946.

spectrum was fitted with a model of ($\text{TBABS}_{(CXB)} \times \text{PL}_{(CXB)} + \text{APEC}_{(FE)} + \text{TBABS}_{(GH)} \times (\text{APEC}_{(GH-hot)} + \text{APEC}_{(GH-cold)})$). The best-fit parameters and spectrum of the background are given in Table 2 and Figure 2, respectively.

The background region for RCW 86 was extracted from a circular area of 58.63 arcmin$^2$ in the same FoV (as seen in Figure 3). The spectrum was fitted with a model of ($\text{TBABS}_{(CXB)} \times \text{PL}_{(CXB)} + \text{APEC}_{(FE)}$). The best-fit parameters and spectrum of the background are given in Table 3 and Figure 3, respectively.

The background region for RX J1713.7 − 3946 was extracted from an area of 77.52 arcmin$^2$ for SW rim and an area of 34.32 arcmin$^2$ for the NW rim in the same FoV, respectively (see top panel of Figure 4). The spectrum of both rims was fitted with a model of ($\text{TBABS}_{(CXB)} \times \text{PL}_{(CXB)} + \text{TBABS}_{(GRXE)} \times (\text{APEC}_{(HP)} + \text{APEC}_{(LP)} + \text{PL}_{(CM)}) + \text{TBABS}_{(FE)} \times (\text{APEC} + \text{APEC})$) as in [5]. The second term is the GRXE component which is represented by a 2-CIE model, a high-temperature plasma (7 keV) plus a low-temperature plasma (1

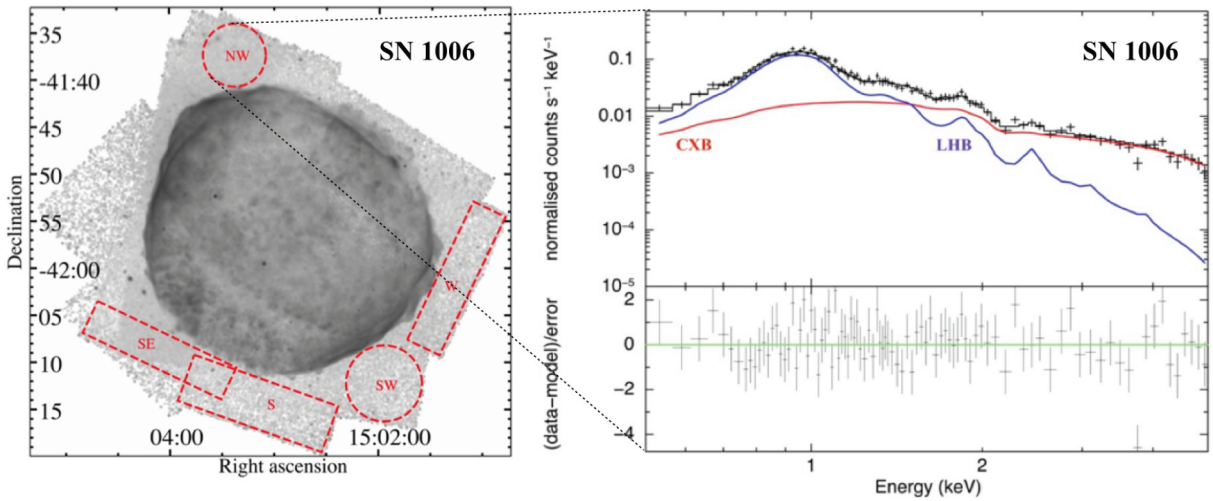



**Figure 5**. *Left*: The selected background regions for SN 1006. *Right*: The background spectrum exemplified with the NW rim of SN 1006. All selected background regions for SN 1006 show the same characteristic.

**Table 4**. Best-fit parameters for the background spectrum of the SW rim of RX J1713.7−3946.

| Components | Parameters | Values |
|---|---|---|
| *CXB* | | |
| | $N_H$ ($10^{22}$ cm$^{-2}$) ⋄ | 1.830 *(fixed)* |
| | Photon index † | 1.412 *(fixed)* |
| | S. B. † (erg s$^{-1}$ cm$^{-2}$ arcmin$^{-2}$) | $5.410 \times 10^{-15}$ *(fixed)* |
| *GRXE* ∗ | | |
| | $N_H$ ($10^{22}$ cm$^{-2}$) | $0.915^{+0.170}_{-0.154}$ |
| | $kT_e$ (keV) | 1.0 *(fixed) (LP)* |
| | Norm ($10^{-2}$ cm$^{-5}$) | $0.014^{+0.030}_{-0.014}$ |
| | $kT_e$ (keV) | 7.0 *(fixed) (HP)* |
| | Norm (cm$^{-5}$) | 0.257 ± 0.001 |
| | Photon index | 2.00 *(fixed) (CM)* |
| | Norm ($10^{-2}$) ‡ | $3.211^{+1.653}_{-1.600}$ |
| *FE* ∗ | | |
| | $N_H$ ($10^{22}$cm$^{-2}$) | 0.56 *(fixed)* |
| | $kT_e$ (keV) | 0.09 *(fixed)* |
| | Norm ($10^{-2}$ cm$^{-5}$) | 0.167 ± 0.018 |
| | $kT_e$ (keV) | 0.59 *(fixed)* |
| | Norm ($10^{-2}$ cm$^{-5}$) | 0.002 ± 0.001 |
| | $\chi^2$ / d.o.f | 461.25 / 438 |

‡: *The normalisation of the power-law is in units of photons cm$^{-2}$ s$^{-1}$ keV$^{-1}$ at 1 keV.*
⋄: $N_{H\,(CXB)} = 2 \times N_{H\,(GRXE)}$ *and* ∗: *[5].*
†: *[17].*

keV) [5], and also with a CM nonthermal component. Because RX J1713.7−3946 emission is under the effect of the GRXE, careful background subtraction is required. Thus, particular attention to background subtraction

**Table 5**. Best-fit parameters for the background spectrum of the NW rim of RX J1713.7−3946.

| Components | Parameters | Values |
|---|---|---|
| *CXB* | | |
| | $N_H$ ($10^{22}$ cm$^{-2}$) ⋄ | 1.355 *(fixed)* |
| | Photon index † | 1.412 *(fixed)* |
| | S. B. † (erg s$^{-1}$ cm$^{-2}$ arcmin$^{-2}$) | $5.410 \times 10^{-15}$ *(fixed)* |
| *GRXE* ∗ | | |
| | $N_H$ ($10^{22}$ cm$^{-2}$) | $0.677 \pm 0.024$ |
| | $kT_e$ (keV) | 1.0 *(fixed) (LP)* |
| | Norm ($10^{-2}$ cm$^{-5}$) | $0.035^{+0.041}_{-0.030}$ |
| | $kT_e$ (keV) | 7.0 *(fixed) (HP)* |
| | Norm ($10^{-3}$ cm$^{-5}$) | $0.844 \pm 0.040$ |
| | Photon index | 2.00 *(fixed) (CM)* |
| | Norm ($10^{-2}$) ‡ | $8.15^{+0.834}_{-0.653}$ |
| *FE* ∗ | | |
| | $N_H$ ($10^{22}$cm$^{-2}$) | 0.56 *(fixed)* |
| | $kT_e$ (keV) | 0.09 *(fixed)* |
| | Norm (cm$^{-5}$) | $0.135 \pm 0.013$ |
| | $kT_e$ (keV) | 0.59 *(fixed)* |
| | Norm ($10^{-4}$ cm$^{-5}$) | $0.144 \pm 0.011$ |
| | $\chi^2$ / d.o.f | 395.52 / 439 |

‡: *The normalisation of the power-law is in units of photons cm$^{-2}$ s$^{-1}$ keV$^{-1}$ at 1 keV.*
⋄: $N_{H\,(CXB)} = 2 \times N_{H\,(GRXE)}$ *and* ∗: *[5].*
†: *[17].*

was paid with reanalysing of the Chandra data. The third term is the absorbed FE, which is represented with optically thin thermal plasma, and fixed component values as in [5] ($N_{H\,(FE)} = 5.6 \times 10^{21}$ cm$^{-2}$, $kT_e = 0.09$ keV and 0.59 keV). The best-fit parameters and the spectra of the background regions are shown in Table 4, Table 5, and Figure 4, respectively.

Figure 5 shows ACIS-I and ACIS-S mosaic images of the data of ObsId: 732, 1959, 3838, 4385, 4394, 9107, 13737, 13738, 13739, 13741, 13742, 13743, 14423, 14424, 14435 (which include NW, S, SE, SW, and W rims of SN 1006). For all rims, the background spectra were chosen from the source-free regions in the same FoV (Figure 5). The background spectra of all rims were fitted with a model of (TBABS$_{(CXB)}$ × PL$_{(CXB)}$ + APEC$_{(LHB)}$). The contribution of the LHB to the X-ray spectrum is determined in [22]. The column density was fixed at $6.8 \times 10^{20}$ cm$^{-2}$ following the H I observation in [32]. The best-fit parameters and the spectra of the background regions are shown in Table 6 and Figure 5, respectively.

## 4. Results and discussion

In this study, the spectral analysis was performed for the source-free regions on the observations of four SNRs (Cas A, RCW 86, RX J1713.7−3946, and SN 1006) to mention the background analysis methods briefly. As mentioned in the previous sections, we concentrated upon the accurate background modelling for the analysis

**Table 6**. Best-fit parameters for the background spectrum of the NW rim of SN 1006.

| Components | Parameters | Values |
|---|---|---|
| *CXB* | | |
| | $N_H$ ($10^{22}$ cm$^{-2}$) ‡ | 0.068 *(fixed)* |
| | Photon index † | 1.412 *(fixed)* |
| | S. B. † (erg s$^{-1}$ cm$^{-2}$ arcmin$^{-2}$) | $5.410 \times 10^{-15}$ *(fixed)* |
| *LHB* | | |
| | $kT_e$ (keV) | $0.987 \pm 0.014$ |
| | Norm ($10^{-2}$ cm$^{-5}$) | $0.025 \pm 0.001$ |
| | $\chi^2$ / d.o.f | 388.56 / 442 |

†: *[17]*. ‡:*[32]*.

of an extended source to lay emphasis on estimating the reliable values of spectral parameters. Despite the effect of the CXB is valid for the background emission of all the SNRs as seen in the first lines of all the tables, its contribution differs for each SNR. To calculate the absorbed flux of each component for background spectrum in $0.5-7.0$ keV, we used the convolution model (CFLUX in XSPEC). In Table 7, the contribution of each component is roughly specified as percentage values in the background spectrum for each SNR according to their X-ray flux values.

**Table 7**. The contribution of the components roughly specified as percentage values in the background spectrum for each SNR.

| Component | Cas A | RCW 86 | RX J1713.7−3946 | RX J1713.7−3946 | SN 1006 |
|---|---|---|---|---|---|
| | | | (SW rim) | (NW rim) | |
| CXB | 0.3% | 60.2% | 2.7% | 3.2% | 23.7% |
| FE | 8.2% | 39.8% | ... | ... | ... |
| GH-hot | 25.9% | ... | ... | ... | ... |
| GH-cold | 65.6% | ... | ... | ... | ... |
| FE-hot | ... | ... | 2.3% | 0.1% | ... |
| FE-cold | ... | ... | 7.5% | 5.1% | ... |
| LHB | ... | ... | ... | ... | 76.3% |
| GRXE: HP | ... | ... | 76% | 14.9% | ... |
| GRXE: LP | ... | ... | 0.2% | 3.7% | ... |
| GRXE: CM | ... | ... | 11.4% | 73% | ... |

*Cas A*: The background spectrum of Cas A is dominated by the FE, the GH-cold, and the GH-hot (the most dominant component) as seen in Table 2. Some elemental emission lines can be seen in the spectrum which point out that the X-ray background of the SNR is contaminated by the thermal components in the approximate energies of about 1.83, 2.42, 3.09, 3.87, and 6.61 keV. The GH component which was fixed at the values indicated in [31] has a high absorption value of approximately $2.11 \times 10^{22}$ cm$^{-2}$ compared with the Galactic column density value of the whole SNR. As seen in Figure 2, both GH and FE release the Fe K$\alpha$ line emission on the X-ray background spectrum of Cas A, and the most dominant one comes from the GH-cold.

Since Cas A has complex structured knots and require reliable spectral analysis, in the Chandra studies [33,34,35], the X-ray background emission of Cas A observations was selected carefully from emission-free regions for the spectral analysis but no background estimation method was indicated.

*RCW 86*: RCW 86 has unabsorbed FE in its X-ray background spectra with the $kT_e$ value of approximately 0.70 keV. The flux of the FE in the background spectrum of the SNR is slightly low compared to the indications of it on the other SNRs. As seen in Figure 3, the X-ray background component FE is effective on the low energy side of the spectrum.

Lemoine-Goumard et al. [36] carefully treated the X-ray background emission of RXTE archival data of RCW 86. They pointed out the spatial variations in the CXB in the $10-20$ keV energy band and added power-law component with a spectral photon index of 1.3 to the fit to represent the excess CXB emission. They ignored the emission from the GRXE because it reveals little evidence of Galactic Ridge emission in the $10-25$ keV energy band for the data of this observation.

*RX J1713.7−3946*: Principally, in order to evaluate the possible contamination by the GRXE, the location of the remnant on the Galactic latitude is the first to take into account. RX J1713.7−3946 is on the Galactic plane and only its background spectrum is dominated by the GRXE. The background spectrum of RX J1713.7−3946 consists of the CXB, GRXE, CM, and FE components. As seen in Figure 4, for both SW and NW rims of the SNR, domination of the low-temperature plasma component (1 keV) is very low compared with the high-temperature plasma component (7 keV) in the GRXE (see Table 7).

Moreover, the Galactic plane background includes the FE, which is not enough to dominate in the NW observation. Besides, the influence of the component that is associated with the CM is slightly higher in the SW observation. As seen from the right panel of Figure 4, hot component of the FE is ineffective, which cannot be seen in the spectrum. It can be seen that HP component of the GRXE in both spectra reveals the Fe K$\alpha$ line emission, as expected due to the characteristic of the GRXE [5].

In their XMM-Newton study, Acero et al. [37] extracted the astrophysical X-ray background spectra outside the SNR in four regions (N, NW, SW, and SE) and then, estimated it with a power-law model instead of a spectrum but did not mention any thermal model for the GRXE. Hiraga et al. [38] pointed out the importance of the background estimation for the extended sources in their XMM-Newton study and represented it to be the blend of CXB, nonX-ray background (NXB) and the Galactic diffuse emission. Considering that the SNR is interacting with the molecular clouds according to its Galactic location, they estimated the astrophysical X-ray background with absorbed power-law component with varying spectral photon indices of approximately 2.28 and approximately 2.38 for the NW and SW rims, respectively. On the other hand, in their joint spectral analysis of the archival data from ROSAT PSPC, ASCA GIS, and RXTE PCA observations, Pannuti et al. [39] estimated the background diffuse X-ray emission from the Galactic ridge as observed by the RXTE PCA with POWER-LAW + RAYMOND model, and fixed the values for $kT_e$, spectral photon index, and $N_H$ to be 2.9 keV, 1.8, and $1.8 \times 10^{22}$ cm$^{-2}$, respectively. They also argued about the spectral feature seen near 6.4 keV, whether it is associated with the SNR or the diffuse emission associated with the Galactic Ridge.

*SN 1006*: The selected background regions of SN 1006 include nonthermal emission from the CXB and unabsorbed emission contribution from the LHB, which is dominant in comparison with the CXB (see Table 7).

Using the XMM-Newton archival data, Li et al. [40] extracted and fitted the astrophysical X-ray background spectra with VMEKAL + POWER-LAW model. The thermal plasma component represents the LHB emission, whose $kT_e$ value was fixed at 0.1 keV. In our study, we let the temperature of the LHB to vary freely and derived $kT_e$ approximately 0.987 keV. The nonthermal component, POWER-LAW, is for generating

the possible contribution from the scattered light of the nonthermal arcs and the cosmic background with a photon index of approximately $1.4-1.7$. In another XMM-Newton study, using the standard ESAS method of background subtraction, Miceli et al. [41] developed a procedure similar to the double background-subtraction technique. They modelled the background spectra in Xspec and put these parameters associated with the background emission fixed when fitting the source spectra.

## 5. Conclusion

We summarise the main results of our spectral analyses of the source-free emission regions of the well-known shell-type Galactic SNRs Cas A, RCW 86, RX J1713.7−3946, and SN 1006 with the archival data from Chandra and XMM-Newton X-ray Observatories to briefly represent the X-ray background estimation method as follows:

1. We have found the following components in the estimated X-ray background spectrum of Cas A, which is combined with the thermal and nonthermal models: CXB (nonthermal), GH (absorbed thermal), and FE (unabsorbed thermal). The Galactic location of Cas A is the determinant of the existence of the component GH, which is why it is not found in other SNRs in our study but in Cas A located in the $2^{nd}$ quadrant of the Galaxy. According to its X-ray flux value, the cold component of the GH is the most dominant one in the background spectrum of Cas A ($\sim$65.6%).

2. RCW 86 has unabsorbed FE in its X-ray background spectra with the $kT_e$ value of $0.703 \pm 0.014$ keV. The FE domination in the spectrum of the SNR is approximately 39.8%.

3. The X-ray background emission of RX J1713.7−3946 contains CXB, GRXE, and absorbed FE. The Galactic location of RX J1713.7−3946 is the determinant of the existence of the GRXE; the SNR is located in the $4^{th}$ quadrant of the Galaxy. For the SW rim of the SNR, the background emission from the HP is the most dominant component ($\sim$76%), while for the NW rim of the SNR, CM is the most dominant one ($\sim$73%).

4. SN 1006 is far above the Galactic plane; thus, the contribution of the GRXE to the spectra is negligible as mentioned in Section 3.1. The X-ray background emission for SN 1006 involves the CXB ($\sim$23.7%) and the unabsorbed LHB emission ($\sim$76.3%) with an average $kT_e$ value of approximately 0.95 keV.

## Acknowledgments

This study is supported by the YTU Scientific Research and Project Office (BAP) funding with contract numbers FYL-2018-3309.

## References

[1] Doroshenko, V.; Pühlhofer, G.; Bamba, A.; Acero, F.; Tian, W. W.; Klochkov, D.; Santangelo, A. *Astron. Astrophys.* **2017**, *608*, preprint, (arXiv:1708.04110).

[2] Yasumi, M.; Nobukawa, M.; Nakashima, S.; Uchida, H.; Sugawara, R.; Tsuru, T.; Tanaka, T. ; Koyama, K. *Publ. Astron. Soc. Jpn.* **2014**, *66*, 68.

[3] Sato, T.; Koyama, K.; Takahashi, T.; Odaka, H.; Nakashima, S. *Publ. Astron. Soc. Jpn.* **2014**, *66*, 124.

[4] Yuasa, T.; Makishima, K.; Nakazawa, K. *Astrophys. J.* **2012**, *753*, 1-16.

[5] Uchiyama, H.; Nobukawa, M.; Tsuru, T.; Koyama, K. *Publ. Astron. Soc. Jpn.* **2013**, *65*, 19.

[6] Katsuda, S.; Acero, F.; Tominaga, N.; Fukui, Y.; Hiraga, J.; Koyama, K.; Lee, S.; Mori, K.; Nagataki, S.; Ohira, N. et al. *Astrophys. J.* **2015**, *814*, 1-11.

[7] Haslam, C. G. T.; Salter, C. J.; Stoffel, H.; Wilson, W. E. *Astrophys. J. Suppl. S.* **1982**, *1, 2*, 4-51, 53-142.

[8] Ebisawa, K.; Maeda, Y.; Kaneda, H.; Yamauchi, S. *Science* **2001**, *293*, 1633-1635.

[9] Ebisawa, K.; Tsujimoto, M.; Paizis, A.; Hamaguchi, K.; Bamba, A.; Cutri, R.; Kaneda, H.; Maeda, Y.; Sato, G.; Senda, A. et al. *Astrophys. J.* **2005**, *635*, 214-242.

[10] Ebisawa, K.; Yamauchi, S.; Tanaka, Y.; Koyama, K.; Ezoe, Y.; Bamba, A.; Kokubun, M.; Hyodo, Y.; Tsujimoto, M.; Takahashi, H. *Publ. Astron. Soc. Jpn.* **2008**, *60*, 223-230.

[11] Kaneda, H.; Makishima, K.; Yamauchi, S.; Koyama, K.; Matsuzaki, K.; Yamasaki, N. Y. *Astrophys. J.* **1997**, *491*, 638-652.

[12] Nobukawa, M.; Koyama, K.; Tsuru, T. G.; Ryu, S. G.; Tatischeff, V. *Publ. Astron. Soc. Jpn.* **2010**, *62*, 423-429.

[13] Yuasa, T. *Suzaku Studies of White Dwarf Stars and the Galactic X-ray Background Emission*; Springer: Tokyo, Japan, 2013.

[14] Kamitsukasa, F.; Koyama, K.; Uchida, H.; Nakajima, H.; Hayashida, K.; Mori, K.; Katsuda, S.; Tsunemi, H. *Publ. Astron. Soc. Jpn.* **2015**, *67*, 16.

[15] Bamba, A.; Terada, Y.; Hewitt, J.; Petre, R.; Angelini, L.; Safi-Harb, S.; Zhou, P.; Bocchino, F.; Sawada, M. *Astrophys. J.* **2016**, *818*, 1-11.

[16] Moretti, A.; Pagani, C.; Cusumano G.; Campana, S.; Perri, M.; Abbey, A.; Ajello, M.; Beardmore, A. P.; Burrows, D.; Chincarini, G. et al. *Astron. Astrophys.* **2009**, *493*, 501-509.

[17] Kushino, A.; Ishisaki, Y.; Morita, U.; Yamasaki, N. Y.; Ishida, M.; Ohashi, T.; Ueda, Y. *Publ. Astron. Soc. Jpn.* **2002**, *54*, 327-352.

[18] Cappelluti, N.; Li, Y.; Ricarte, A.; Agarwal, B.; Allevato, V.; Tasnim A. T.; Ajello, M.; Civano, F.; Comastri, A.; Elvis, M. et al. *Astrophys. J.* **2017**, *837*, 1-8.

[19] Ryu, S. G.; Koyama, K.; Nobukawa, M.; Fukuoka, R. T.; Takeshi G. *Publ. Astron. Soc. Jpn.* **2009**, *61*, 751-761.

[20] Henley, D. B.; Shelton, R. L. *Astrophys. J.* **2013**, *773*, 1-21.

[21] Henley, D. B.; Shelton, R. L. *Astrophys. J.* **2015**, *808*, 1-28.

[22] Liu, W.; Chiao, M.; Collier, M. R.; Cravens, T.; Galeazzi, M.; Koutroumpa, D.; Kuntz, K. D.; Lallement, R.; Lepri, S. T.; McCammon, D. et al. *Astrophys. J.* **2017**, *834*, 1-6.

[23] Sawada, M. PhD, Department of Physics, Kyoto University, Kyoto, Japan, 2011.

[24] Henley, D.B.; Shelton, R. L.; Kuntz, K. D. *Astrophys. J.* **2007**, *661*, 304-319.

[25] Matsumura, H.; Uchida, H.; Tanaka, T.; Tsuru, T. G.; Nobukawa, M.; Nobukawa, K. K.; Itou, M. *Publ. Astron. Soc. Jpn.* **2017**, *69*, 1-8.

[26] Yoshino, T.; Mitsuda, K.; Yamasaki, N.Y.; Takei, Y.; Hagihara, T.; Masui, K.; Bauer, M.; McCammon, D.; Fujimoto, R.; Wang, Q. D.; Yao, Y. *Publ. Astron. Soc. Jpn.* **2009**, *61*, 805-823.

[27] Grondin, M.-H.; Sasaki, M.; Haberl, F.; Pietsch, W.; Crawford, E. J.; Filipović, M. D.; Bozzetto, L. M.; Points, S.; Smith, R. C. *Astron. Astrophys.* **2012**, *539*, 1-8.

[28] Kavanagh, P. J.; Sasaki, M.; Whelan, E. T.; Maggi, P.; Haberl, F.; Bozzetto, L. M.; Filipović, M. D.; Crawford, E. J. *Astron. Astrophys.* **2015**, *579*, 1-7.

[29] Wilms, J.; Allen, A.; McCray, R. *Astrophys. J.* **2000**, *542*, 914-924.

[30] Kalberla, P. M. W.; Burton, W. B.; Hartmann, D.; Arnal, E. M.; Bajaja, E.; Morras, R.; Pöppel, W. G. L. *Astron. Astrophys.* **2005**, *440*, 775-782.

[31] Masui, K.; Mitsuda, K.; Yamasaki, N. Y.; Takei, Y.; Kimura, S.; Yoshino, T.; McCammon, D. *Publ. Astron. Soc. Jpn.* **2008**, *61*, 115-122.

[32] Krivonos, R.; Revnivtsev, M.; Churazov, E.; Sazonov, S.; Grebenev, S.; Sunyaev, R. *Astron. Astrophys.* **2007**, *475*, 775-784.

[33] Lee, J.; Park, S.; Hughes, J. P.; Slane, P. O. *Astrophys. J.* **2014**, *789*, 1-11.

[34] Rutherford, J.; Dewey, D.; Figueroa-Feliciano, E.; Heine, S. N. T.; Bastien, F. A.; Sato, K.; Canizares, C. R. *Astrophys. J.* **2014**, *769*, 1-19.

[35] Bamba, A.; Yamazaki, R.; Yoshida, T.; Terasawa, T.; Koyama, K. *Astrophys. J.* **2005**, *621*, 793-802.

[36] Lemoine-Goumard, M.; Renaud, M.; Vink, J.; Allen, G. E.; Bamba, A.; Giordano, F.; Uchiyama, Y. *Astron. Astrophys.* **2012**, *545*, 1-9.

[37] Acero, F.; Ballet, J.; Decourchelle, A.; Lemoine-Goumard, M.; Ortega, M.; Giacani, E.; Dubner, G.; Cassam-Chenaï, G. *Astron. Astrophys.* **2009**, *505*, 157-167.

[38] Hiraga, J. S.; Uchiyama, Y.; Takahashi, T.; Aharonian, F. A. *Astron. Astrophys.* **2012**, *431*, 953-961.

[39] Pannuti, T. G.; Allen, Glenn E.; Houck, John C.; Sturner, S. J. *Astrophys. J.* **2003**, *593*, 377-392.

[40] Li, J.; Decourchelle, A.; Miceli, M.; Vink, J.; Bocchino, F. *Mon. Not. R. Astron. Soc.* **2015**, *453*, 3953-3974.

[41] Miceli, M.; Bocchino, F.; Iakubovskyi, D.; Orlando, S.; Telezhinsky, I.; Kirsch, M. G. F.; Petruk, O.; Dubner, G.; Castelletti, G. *Astron. Astrophys.* **2009**, *501*, 239-249.